Biomech Model Mechanobiol (2015) 14:1335–1347
DOI 10.1007/s10237-015-0677-x

ORIGINAL PAPER

Mechanical properties of normal versus cancerous breast cells

Amanda M. Smelser[1] · Jed C. Macosko[1,2] · Adam P. O'Dell[2] · Scott Smyre[2] · Keith Bonin[2] · George Holzwarth[2]

Received: 22 November 2014 / Accepted: 4 April 2015 / Published online: 1 May 2015

Abstract A cell's mechanical properties are important in determining its adhesion, migration, and response to the mechanical properties of its microenvironment and may help explain behavioral differences between normal and cancerous cells. Using fluorescently labeled peroxisomes as microrheological probes, the interior mechanical properties of normal breast cells were compared to a metastatic breast cell line, MDA-MB-231. To estimate the mechanical properties of cell cytoplasms from the motions of their peroxisomes, it was necessary to reduce the contribution of active cytoskeletal motions to peroxisome motion. This was done by treating the cells with blebbistatin, to inhibit myosin II, or with sodium azide and 2-deoxy-D-glucose, to reduce intracellular ATP. Using either treatment, the peroxisomes exhibited normal diffusion or subdiffusion, and their mean squared displacements (MSDs) showed that the MDA-MB-231 cells were significantly softer than normal cells. For these two cell types, peroxisome MSDs in treated and untreated cells converged at high frequencies, indicating that cytoskeletal structure was not altered by the drug treatment. The MSDs from ATP-depleted cells were analyzed by the generalized Stokes–Einstein relation to estimate the interior viscoelastic modulus G^* and its components, the elastic shear modulus G' and viscous shear modulus G'', at angular frequencies between 0.126 and 628 rad/s. These moduli are the material coefficients that enter into stress–strain relations and relaxation times in quantitative mechanical models such as the poroelastic model of the interior regions of cancerous and non-cancerous cells.

Keywords Particle tracking · Peroxisomes · Actin · Cytoskeleton · Brownian motion · GSE

1 Introduction

Cells' mechanical properties influence how they deform, adhere, and sense the mechanical properties of their microenvironment. A better understanding of cell mechanics and migration may lead to novel treatments of diseases, such as metastatic cancer (Suresh 2007; Butcher et al. 2009; Schedin and Keely 2011). Breast cells are an attractive model for mechanics studies because mammary gland formation and function depend on dynamic microenvironment mechanics, and normal cells from primary human breast tissue and well-characterized, transformed cancerous breast cells are both readily available (Elenbaas et al. 2001; Paszek et al. 2005; Nagaraja et al. 2006; Butcher et al. 2009; Schedin and Keely 2011). The primary question addressed in this paper is "Do the shear moduli G^*, G' and G'' of normal human breast cells differ from the moduli of cancerous breast cell types that are in progressive stages of neoplastic transformation?"

These experiments were designed to compare the interior mechanical properties of normal, tumorigenic, and metastatic breast cells. For "normal breast cells," human mammary epithelial (HME) cells were used at low passage number. To represent non-metastatic, "tumorigenic breast cells," we acquired HME cells that were stably transfected with *hTERT*, oncogenic H-*ras*V12, and the SV40 large-T onco-

Electronic supplementary material The online version of this article (doi:10.1007/s10237-015-0677-x) contains supplementary material, which is available to authorized users.

✉ George Holzwarth
gholz@wfu.edu

[1] Department of Biochemistry and Molecular Biology, Wake Forest University School of Medicine, Winston-Salem, NC 27157, USA

[2] Department of Physics, Wake Forest University, Winston-Salem, NC 27109, USA

gene (Elenbaas et al. 2001). The *hTERT* gene encodes a telomerase subunit which maintains telomeres for indefinite cell division, the SV40 large-T oncogene inactivates the p53 and pRB tumor suppressor pathways, and H-*ras*V12 provides constitutive mitogenic signaling (Elenbaas et al. 2001). Notably, oncogenic Ras also leads to the disruption of stress fibers (Choi and Helfman 2013). Finally, the MDA-MB-231 cell line was selected to represent breast cells with high metastatic potential, hereafter "metastatic breast cells." For convenience, we refer collectively to the tumorigenic and metastatic cells as "cancerous breast cells" throughout the remainder of the paper.

Several techniques are being used to determine the moduli E, G^*, G', and G'' of cells, where E refers to the Young's modulus. Techniques that probe from the outside, including atomic force microscopy (AFM), micropipette aspiration, and magnetic twisting cytometry, appear to measure the modulus of the cell cortex, which is composed primarily of actin fibers (Hoffman et al. 2006). By contrast, active and passive particle-tracking microrheology measures the moduli of the cell interior (Hoffman et al. 2006; Bursac et al. 2005; Gal and Weihs 2012; Wirtz 2009; Bertseva et al. 2012; Guo et al. 2013). Within the context of a poroelastic model (Moeendarbary et al. 2013), the external probes measure the mechanical properties of the porous elastic solid phase, while microrheology measures the moduli of the crowded interstitial fluid and its smaller cytoskeletal components, which are the poroelastic fluid phase. The moduli determined by the two experimental approaches differ by several orders of magnitude because they measure the mechanical properties of different components of the cell. The experiments presented here use passive microrheology to determine the mechanical properties of the interstitial fluid phase within normal and metastatic breast cells.

The passive probes used in these experiments were fluorescently labeled peroxisomes. These ubiquitous organelles are involved in fatty acid catabolism and neutralization of harmful cellular by-products such as hydrogen peroxide. They were labeled by transducing cells with a construct whose expression generates GFP fused to a peroxisomal targeting sequence (Invitrogen). Peroxisomes have several advantageous features as rheological probes: They are endogenous, thus minimizing cell perturbation; are approximately spherical, which simplifies the analysis; have a relatively narrow size distribution; are rarely actively transported, which would violate assumptions of the analysis; and are rich in antioxidant enzymes, which may reduce photobleaching of the GFP.

Three sources of peroxisome motion have been identified in cells: (a) directed, ATP-driven motion, (b) ATP-driven random motion, and (c) thermally driven random motion. Figure 1a, b, and c shows these three processes pictorially. Only a small fraction (5–15 %) of peroxisomes experience "saltatory, fast directional movement" (Wiemer et al. 1997; Schrader et al. 2000, 2003). Such fast directional motion (Fig. 1a) is caused by kinesin- or dynein-driven transport of the peroxisomes along microtubules (Rapp et al. 1996; Wiemer et al. 1997; Schrader et al. 2000, 2003; Kural et al. 2005). Random peroxisome motion, on the other hand, can arise from ATP-driven cytoskeletal motion (Fig. 1b) or by thermal energy (true Brownian motion, Fig. 1c) (Hoffman et al. 2006; Bursac et al. 2005; Van Citters et al. 2006; Bursac et al. 2007; Mizuno et al. 2007; Brangwynne et al. 2008, 2009; Gallet et al. 2009).

A number of experimental and data-processing approaches have been developed to determine whether a track, or a segment of a track, is type a, b, or c. For peroxisomes in breast cells, type a motion is rare and obvious to the

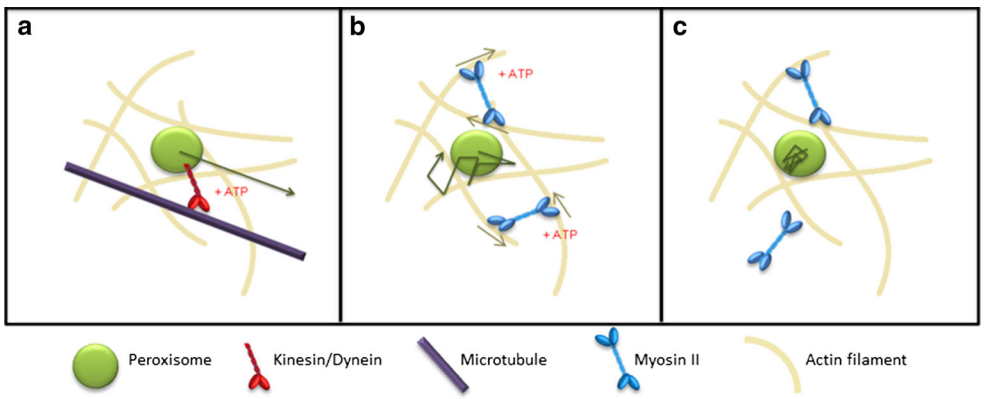

Fig. 1 Three sources of peroxisome motion. **a** *Directed motion* occurs when ATP-powered kinesin or dynein motors pull the peroxisomes along microtubules. **b** *ATP-driven but random motion* leads to cytoskeletal filament motion which indirectly contributes to peroxisome motion. Myosin II activity between actin filaments is shown; **c** *Thermally driven random motion* is the sole source of random peroxisome motion if all direct and indirect ATP-powered processes can be shut down

eye, so such tracks can be manually identified or detected by image processing. However, separation of type b from type c motions is difficult and controversial, because both types are random in direction. One approach is to treat cells with sodium azide and 2-deoxy-D-glucose. Sodium azide inhibits the enzymes necessary for oxidative phosphorylation (Ishikawa et al. 2006) and 2-deoxy-D-glucose inhibits glycolysis (Wick et al. 1957). Used together, cellular ATP levels can be reduced to 1–8 % of normal in breast cells. If active cellular processes are sufficiently suppressed by such treatment, the remaining random peroxisome motion is due primarily to thermal energy (Bursac et al. 2005; Hoffman et al. 2006; Gallet et al. 2009; Guo et al. 2014a). In this case, the viscoelastic modulus of the cytoplasm can be determined from the mean square displacements (MSDs) and the generalized Stokes–Einstein equation (Mason 2000; Squires and Mason 2010).

Use of the GSE equation to determine G' and G'' of live cells in this way is controversial. The major criticism has been that treatment of cells with sodium azide or blebbistatin cannot possibly remove all non-thermal contributions to the MSD without causing significant damage to the cells (Gal et al. 2013). We addressed this concern in three ways. First, we measured the effects of two azide concentrations and three blebbistatin concentrations on the MSDs and apparent G^* values. Second, we used the convergence of the MSDs of peroxisomes in treated and untreated cells at high frequencies as a test of whether cell damage was significant (Mizuno et al. 2007; Guo et al. 2014a). If the MSDs converged, we used the GSE equation to evaluate G^*, G', and G'' by GSE for that cell line. If the MSDs did not converge, the GSE equation was not applied. Third, where published data are available, we have compared our moduli to moduli obtained by active microrheology, which does not depend on the use of GSE or drug treatment. Although agreement is not perfect, it is close, given that the cell lines are not identical. Our view is that useful data can be obtained from GSE analysis in this way.

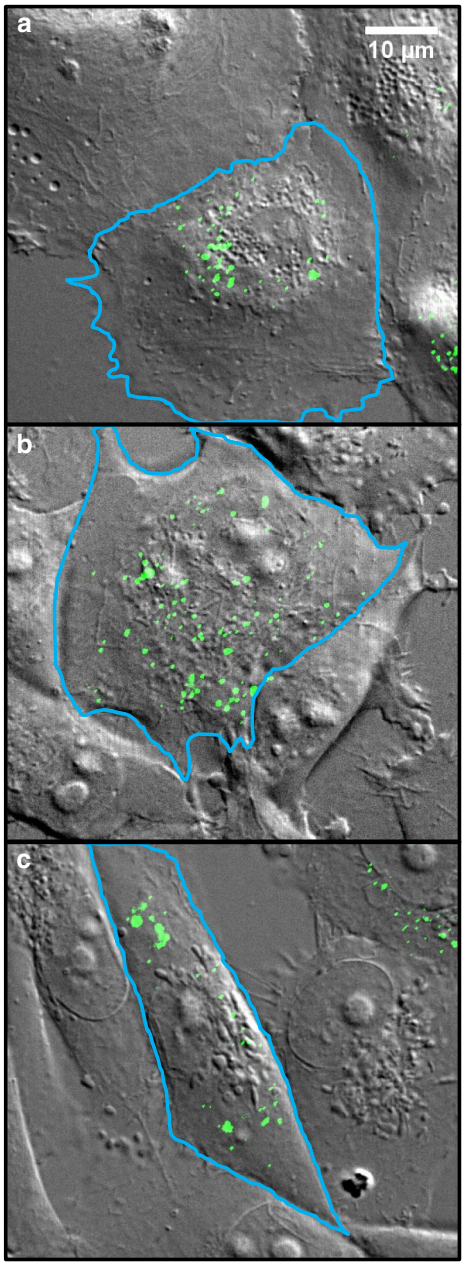

Fig. 2 Overlay of DIC and fluorescence images to show cell morphologies and peroxisome distribution in **a** normal, **b** tumorigenic, and **c** metastatic breast cells, all grown on laminin–collagen-coated glass surfaces. The DIC images (*grayscale*) show an entire cell and several of its neighbors; the edge of the cell is labeled with a *blue line*. GFP-labeled peroxisomes appear as punctate *green spots* in the overlaid fluorescence image. The *scale bar* shown in (**a**) applies to (**b**) and (**c**) as well

2 Methods

2.1 Cell culture

Normal HME cells were obtained from Lonza (Walkersville, MD). Tumorigenic non-metastatic human mammary epithelial (HMLER) cells developed in the Weinberg laboratory (Elenbaas et al. 2001) were provided by Karin Scarpinato. Metastatic HME (MDA-MB-231) cells were obtained from the American Type Culture Collection (ATCC, Manassas, VA). Normal, tumorigenic, and metastatic breast cells were cultured in mammary epithelial growth medium (MEGM) supplemented with 0.4 % bovine pituitary extract (Lonza) at 37 °C with 5 % CO_2. Two or three days before imaging, either 80,000 (normal and metastatic) or 160,000 (tumorigenic) cells were plated in 35-mm glass-bottom dishes (WillCo Wells, Amsterdam). The dishes were coated with 100 µl of a 33 µg/ml collagen type IV (BD Biosciences, Franklin Lakes, NJ), 67 µg/ml laminin mixture (Engelbreth-Holm-Swarm murine sarcoma, Sigma-Aldrich, St Louis, MO) to mimic the composition of a basement membrane. To fluorescently

label peroxisomes with GFP, 10 µl BacMam 2.0 peroxisome-GFP reagent (Life Technologies, Carlsbad, CA) was added to each dish 1 day before imaging. Figure 2 shows the morphologies of individual normal, tumorigenic and metastatic cells and the distribution of GFP-labeled peroxisomes.

2.2 Myosin II inhibition and ATP depletion

To test for the presence of ATP-driven motion in the MSDs of peroxisomes, cells were treated on imaging days with either (−)-blebbistatin (Sigma-Aldrich), a specific inhibitor of myosin II (Limouze et al. 2004; Kovacs et al. 2004; Allingham et al. 2005) or sodium azide (Sigma-Aldrich) and 2-deoxy-D-glucose (Sigma-Aldrich), which together inhibit cellular ATP production by inhibiting enzymes necessary for oxidative phosphorylation (Ishikawa et al. 2006) and glycolysis (Wick et al. 1957), respectively. Blebbistatin was dissolved in dimethylsulfoxide (DMSO, Sigma-Aldrich) at a concentration of 2.5 mM, then diluted into MEGM so that final cell treatment concentrations were 2.5, 5, and 10 µM in 0.1, 0.2, and 0.4 % DMSO, respectively. Control cells were treated with 0.4 % DMSO. Blebbistatin-treated cells were imaged 15 min to 1 h after treatment. For ATP depletion experiments, other cells were treated with media or one of two concentrations of sodium azide and 2-deoxy-D-glucose 3–6 h before imaging. Cells were either treated with 2 mM sodium azide and 2 mM 2 deoxy-D-glucose (hereafter, "low azide") or 8 mM sodium azide and 50 mM 2-deoxy-D-glucose ("high azide"), since both of these concentrations have been used for ATP depletion in previous studies of active cytoskeletal motion (Bursac et al. 2005; Hoffman et al. 2006).

The morphologies of normal cells appeared unaffected by sodium azide and 2-deoxy-D-glucose. The tumorigenic cells appeared more rounded when treated with high azide. Similarly, the metastatic cells rounded up in high azide.

2.3 Fluorescence videomicroscopy

Cells were maintained at 37 °C and 5 % CO_2 while being imaged by a Nikon Eclipse T*i* inverted epifluorescence microscope using a 60× NA 1.4 oil-immersion objective. DIC images were acquired using the same objective, and the condenser for these was NA 0.9 (WI). Illumination was provided by an X-Cite 120 mercury arc lamp with a FITC fluorescence cube. Three fields of view were imaged per dish of cells. To reduce GFP photobleaching but still acquire images over 100 s, an automated shutter (Uniblitz VS25, Vincent Associates) was inserted into the fluorescence excitation light path, so that the dish was illuminated in ten 1-s bursts separated by nine 9-s dark intervals. A high-speed scientific CMOS camera (pco.edge, PCO, Kelheim, Germany, 6.5 µm × 6.5 µm pixel size) was synchronized with the shutter by two linked Tektronix 5101 Arbitrary Function Generators to acquire 100 images during each 1-s burst. This shuttering scheme gave MSDs with τ values between 0.01 and 1 s and between 10 and 90 s but left a gap between 1 and 10 s.

2.4 Peroxisome tracking to determine MSD and modulus

Individual peroxisomes were tracked to subpixel precision, using Video Spot Tracker software (CISSM, University of North Carolina, Chapel Hill, NC). Online Resource 1 is a short movie showing random motion of several peroxisomes and the software's ability to track one of them. The coordinates were then processed by customized MATLAB software (The Mathworks, Natick, MA) to remove stage drift and/or cell migration artifacts from peroxisome tracks and then determine the mean MSDs of each peroxisome. For drift removal, the mean x- and y-coordinates of all peroxisomes in a field of view or migrating group of cells was subtracted from the raw peroxisome coordinates, for each frame. Time-averaged MSDs, $\Delta r^2(\tau)$, were determined from these drift-corrected tracks, as follows:

$$\Delta r^2(\tau) = \langle [x(t+\tau) - x(t)]^2 + [y(t+\tau) - y(t)]^2 \rangle \quad (1)$$

where τ is 0.01 to 90 s. Peroxisome MSDs from sodium azide or blebbistatin-treated cells were used to determine $|G^*|$, the magnitude of the viscoelastic modulus (G^*), using Mason and Weitz's generalization of the Stokes–Einstein equation (GSE) as follows:

$$|G^*(\omega)| = \frac{2k_B T}{3\pi R \Delta r^2\left(\frac{1}{\omega}\right) \Gamma[\alpha(\omega)+1]} \quad (2)$$

where k_B is Boltzmann's constant, T is temperature in K, R is the radius of the peroxisome, ω is the angular frequency $2\pi/\tau$, α is the slope of the log–log plot of the average MSDs vs. τ, and Γ is the gamma function (Mason 2000; Squires and Mason 2010). This equation employs a Laplace transform that converts the MSD time domain range of 0.01–90 s to a frequency domain range of 0.126–628 rad/s for computed values of G^*.

The value of the peroxisome radius was determined by fitting a 2D symmetrical Gaussian to the fluorescent intensities, $I(x, y)$, of individual peroxisomes (Online Resource 2) as follows:

$$I(x, y) = Ae^{-\frac{(x_0-x)^2+(y_0-y)^2}{2\sigma^2}} - b \quad (3)$$

where x_0 and y_0 locate the center of the Gaussian, σ is the width of the Gaussian, A is its amplitude, and b is its baseline. The width of the Gaussian, σ, was assumed to be a good approximation for R.

The average radius determined from 240 peroxisomes was 191 ± 42 nm; there was no significant difference between the average radii of peroxisomes in different cell types, nor between cells subjected to different treatments. Since this radius was less than the wavelength of light, we checked whether it might have a significant systematic error due to the point spread function (PSF) of the objective lens. The width of a Gaussian approximation to the PSF of a 60× NA 1.4 wide-field objective collecting 509 nm light is 80 nm (Zhang et al. 2007). It is shown in Online Resource 3 that correcting the measured size of peroxisomes for this PSF decreases the mean size from 191 to 179 nm, a change of 7 %. This correction was ignored because of its small value. The elastic (G') and viscous (G'') components of the viscoelastic modulus were determined as follows (Mason 2000):

$$G'(\omega) = |G^*(\omega)| cos\left(\frac{\pi}{2}\alpha(\omega)\right) \quad (4)$$

$$G''(\omega) = |G^*(\omega)| sin\left(\frac{\pi}{2}\alpha(\omega)\right) \quad (5)$$

Software to evaluate G^*, G', and G'' for each peroxisome from measured values of $\Delta r^2(\tau)$ and R (Eq. 2) was written in MATLAB.

2.5 ATP assay

Normal, tumorigenic, and metastatic breast cells were incubated for 3 h in either phenol red-free MEGM (Lonza) as the control condition, or with low azide (2 mM sodium azide and 2 mM deoxy-D-glucose) or high azide (8 mM sodium azide and 50 mM 2-deoxy-D-glucose) added to this MEGM medium. Cells were trypsinized, resuspended in the same media, and assayed in a white 96-well plate (Corning, Corning, NY) using the Adenosine 5′-triphosphate bioluminescent somatic cell assay kit (Sigma-Aldrich cat. no. FLASC). Cell samples were read using a well integration time of 10 s in a Perkin Elmer Enspire 2300 luminometer within 10 min of luciferase/luciferin assay mix addition. The percentage of ATP remaining in low- and high-azide-treated samples was determined from a ratio of their averaged relative luminescence units (RLU) compared to those of control samples. Each cell type and treatment combination was assayed in technical triplicate, and for normal and tumorigenic cells, biological duplicate as well.

After high-azide treatment of the cells on poly-D-lysine-coated flasks, normal cells appeared to have ruffled lamellipodia, and normal, tumorigenic, and metastatic cells did not round up normally upon trypsinization, but peeled off the flask surface retaining their spread morphology.

2.6 Error analysis

2.6.1 Statistical error

For each peroxisome track, a time-averaged MSD was acquired for time intervals τ ranging from 0.01 to 90 s. These time-averaged MSDs were then ensemble-averaged over 94–587 peroxisome tracks. To assure representative sampling, the tracks were acquired from peroxisomes in 21–51 cells over three different experiment days for most conditions. The resultant time and ensemble-averaged MSDs and viscoelastic moduli are shown in Figs. 3, 4, 5, 6 and 7. Error bars shown in these figures are standard error of the mean,

$$\mathrm{SE} = \frac{\sigma}{\sqrt{n}} \quad (6)$$

where σ is the ensemble-averaged standard deviation of peroxisome MSDs or moduli at a given value of τ or frequency for a given condition, and n is the number of peroxisomes analyzed.

The distribution function for the MSD of a particle executing Brownian motion is not a normal distribution (Saxton 1997; Grebenkov 2011). Examination of the distributions of the measured MSDs generated by different peroxisomes in a given cell type and treatment showed pronounced skewness and curtosis; examples are given in Online Resource 5. As a consequence, the statistical significance of differences in the mean MSDs of the three cell types could not be evaluated by the usual Student's t test, which requires normal distributions. However, a two-sample rank procedure such as the Mann–Whitney U test does not require that the data be normally distributed in order to assign a p value (Pratt and Gibbons 1981). The Mann–Whitney procedure in SPSS software (IBM, Armonk, New York) was applied to pairs of MSD distributions to determine whether they were statistically indistinguishable ($p > 0.05$) or significantly different ($p < 0.05$).

In addition, bihistograms of the MSDs (Online Resource 5) were generated to assess whether the distributions were of similar shape. Because they were similar, the Mann–Whitney test was also used to evaluate whether the medians of the MSDs of cell lines were significantly different.

2.6.2 Systematic errors in MSD, G^*, G', and G''

Inspection of Eqs. 2–5 identifies additional possible sources of experimental errors. To evaluate the MSD, one needs a conversion factor between camera pixels and sample xy space. This was determined to three figures with a stage micrometer. Time was determined from frame number and frame rate; frame rate was 100 frames/s; the error was <1 frame/s, 1 %. Thus errors in MSD were largely statistical and were reduced by averaging hundreds of MSDs. Inspection of Eq. 2 shows that the error in G^* is determined by errors in

the MSD and in α, the slope of a log–log plot of MSD versus τ. For a single-particle MSD, the value of α fluctuated unphysically from one value of τ to the next. The unphysical oscillations were eliminated by averaging the MSDs of many particles and then smoothing the averaged MSD with a cubic smoothing spline (MATLAB). These averaged and smoothed values of α were used to obtain G^* from Eq. 2 as well as G' and G'' from Eqs. 4 and 5.

An additional test of our methods, especially software, was provided by tracking the Brownian motion of beads in water, then analyzing the data by our GSE code to check whether the well-documented viscosity of water was recovered. The viscosity was determined from 0.40 μm diameter Fluoresbrite Carboxylate YG polystyrene microspheres (Polysciences, Warrington, PA) suspended in PIPES buffer (80 mM 1,4-piperazinediethanesulfonic acid) supplemented with 7.8 % KCl to match the microsphere density. The measured viscoelastic moduli obtained for beads in buffer matched the values of G^* computed from the handbook value of the viscosity of water at 20 °C ($\eta = 1.00 \times 10^{-3}$ Pa s) (Lemmon 2014). Figure R4 in Online Resource 4 shows the results. The excellent agreement between our experimental method and the well-documented Handbook value is additional evidence that our implementation of particle tracking and GSE works properly in simple systems.

2.6.3 Noise floor

To ensure that the measured MSDs were not contaminated by microscope stage motion or vibration of the detector chip, the noise floor of the system was determined by imaging negatively charged 0.40 μm carboxylate-modified fluorescent beads adhered to the surface of a positively charged aminopropyltriethoxysilane-coated glass-bottom dish. The measured MSD, shown in Fig 3, was 1.0×10^{-4} μm^2 independent of τ. This noise amplitude fell well below the measured MSDs computed from peroxisome position (roughly 10^{-3}–10^{0} μm^2 for all τ) and thus noise from stage and detector vibration contributed minimally to these measurements.

3 Results

3.1 ATP depletion reduced the MSDs of peroxisomes at long timescales

Normal and cancerous breast cells were treated with 0, 2, or 8 mM sodium azide plus 0, 2, or 50 mM 2-deoxy-D-glucose. As described in Materials and Methods, images of the cells were acquired, and peroxisomes in the images were tracked using Video Spot Tracker; tracks exhibiting fast directional movement were discarded. MSDs were calculated from the remaining tracks using Eq. 1, with time interval τ ranging between 0.01 and 90 s. Figure 3 shows the MSDs for the three cell types and three conditions after averaging data from 94 to 519 peroxisomes for each condition. MSDs for the normal cells are shown in Fig. 3a. At $\tau = 0.01$ s, the MSD is approximately 8×10^{-4} μm^2 regardless of the sodium azide and 2-deoxy-D-glucose concentration. This shows that the observed MSD was largely of thermal origin at $\tau = 0.01$ s. In contrast, at longer time intervals, e.g., when $\tau = 90$ s, the MSD dropped from 8×10^{-1} to 6×10^{-3} μm^2 with increasing sodium azide and 2-deoxy-D-glucose concentration (Fig. 3a; Online Resource 6). This means that at large values of τ, the MSDs of peroxisomes in control cells were dominated by

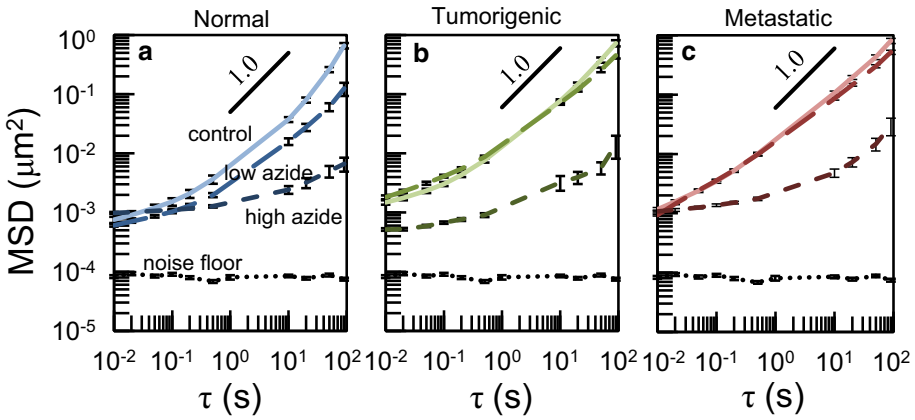

Fig. 3 The effect of ATP depletion on the MSDs of peroxisomes in **a** normal, **b** tumorigenic, and **c** metastatic cells. Cells were either untreated controls (*solid line*), treated with low azide (2 mM sodium azide + 2 mM 2-deoxy-D-glucose, *long dashed line*) or treated with high azide (8 mM sodium azide + 50 mM 2-deoxy-D-glucose, *short dashed line*) in MEGM for 3–6 h. The MSD noise floor was determined by tracking 0.40 μm diameter fluorescent beads adhered to the bottom of a dish. *Error bars* represent standard error of the mean (Eq. 6), where n is the number of peroxisomes (94–519) analyzed for each condition

ATP-driven processes. A similar result is shown for metastatic cells (Fig. 3c).

A luciferase-based ATP assay showed that ATP levels in the cells treated with high azide were only 1–8 % of those of controls. However, ATP levels for low-azide-treated cells were 81–130 % of control ATP levels, which was higher than anticipated. It has been shown that the high-azide treatment leads to rearrangement of the actin cytoskeleton in monkey kidney epithelial cells (Van Citters et al. 2006). On the other hand, the MSDs of peroxisomes in ATP-depleted normal HME cells converged around $\tau = 0.1$s (Fig 3a). This is evidence that the cytoskeleton of these cells was not altered by the treatment with low or high azide (Mizuno et al. 2007; Guo et al. 2014a). Peroxisomes in metastatic cells behaved similarly (Fig 3c). However, peroxisomes in tumorigenic cells (Fig 3b) behaved differently; the MSD did not converge at small values of τ. This suggests that azide treatment caused substantial changes to the cytoskeleton of our tumorigenic cells.

3.2 Myosin II motor inhibition reduced peroxisome MSDs at long timescales

It has been suggested that active peroxisome motion arises from motions of the actin cytoskeleton, and that these motions arise from ATP-powered myosin II motors (Van Citters et al. 2006; Gallet et al. 2009; Brangwynne et al. 2009). To test this hypothesis, we treated all three breast cell types with blebbistatin, a specific inhibitor of myosin II. A dose-dependent decrease in peroxisome MSDs was evident in all three (Fig. 4), supporting the hypothesis that myosin II-driven movement of the actin cytoskeleton is a source of peroxisome motion. As observed with sodium azide and 2-deoxy-D-glucose treatment, blebbistatin did not reduce the MSDs of normal and metastatic cells at short values of τ.

3.3 After inhibition of active processes, peroxisome MSDs were significantly larger in cancerous breast cells than in normal breast cells at long timescales

Figure 5 and Table 1 compare the MSDs of the three cell types treated with azide and blebbistatin at a particular time interval, $\tau = 90$ s. Because the distributions of the MSDs are broad and asymmetric, the Mann–Whitney U test was used to test for significant differences between normal and tumorigenic cells, and between normal and metastatic cells. The results of the Mann–Whitney test are comparable to the impression given by the standard error bars in Fig. 5. In the absence of sodium azide and 2-deoxy-D-glucose treatment, there was no significant difference between MSD distributions in the three cell types (Fig. 5a). These control MSDs are the sum of thermal and ATP-driven contributions. In the presence of low azide, MSDs were reduced in all three cell types, and the difference between MSDs in normal and cancerous cells was statistically significant ($p < 0.005$). In the presence of high azide, MSDs were reduced more dramatically, but remained significantly higher ($p < 0.005$) in metastatic cells than in normal cells (Table 1). The fact that peroxisome MSDs were significantly higher in metastatic cells than in normal cells when active intracellular processes were reduced by ATP depletion suggests that these cells have differences in cytoplasmic mechanical properties, not just differences in motor activity. Specifically, peroxisome motion was less hindered by the cytoplasm in metastatic cells.

In Fig. 5b, the contribution from myosin II activity to the MSDs (the difference between control and 10 μM blebbistatin bars) was larger for the tumorigenic cells than for normal or metastatic cells. Such heightened motor activity in tumorigenic cells has also been observed in MCF-7 cells, another tumorigenic breast cell line (Guo et al. 2014a). In addition, there was a significant increase ($p < 0.005$) in myosin II-independent motion (10 μM blebbistatin bars) from normal to tumorigenic and from normal to metastatic cells (Table 1).

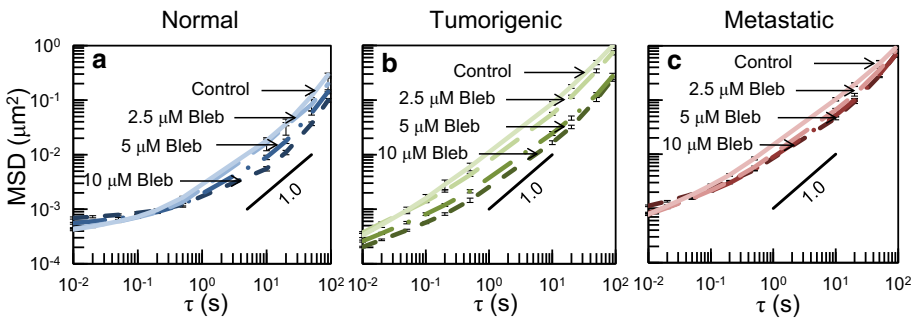

Fig. 4 The dose-dependent effect of myosin II inhibition by blebbistatin on peroxisome MSDs in **a** normal, **b** tumorigenic, **c** metastatic cells. Cells were treated for 15 min–1 h with one of the following in MEGM: (1) 0.4 % dimethylsulfoxide (DMSO) vehicle (*solid line*), (2) 2.5 μM (−)-blebbistatin (*long dashed line*), (3) 5 μM (−)-blebbistatin (*dash-dot*), or (4) 10 μM (−)-blebbistatin (*short dashed line*). *Error bars* represent standard error of the mean (Eq. 6), where n is the number of peroxisomes (177–587) analyzed for each condition

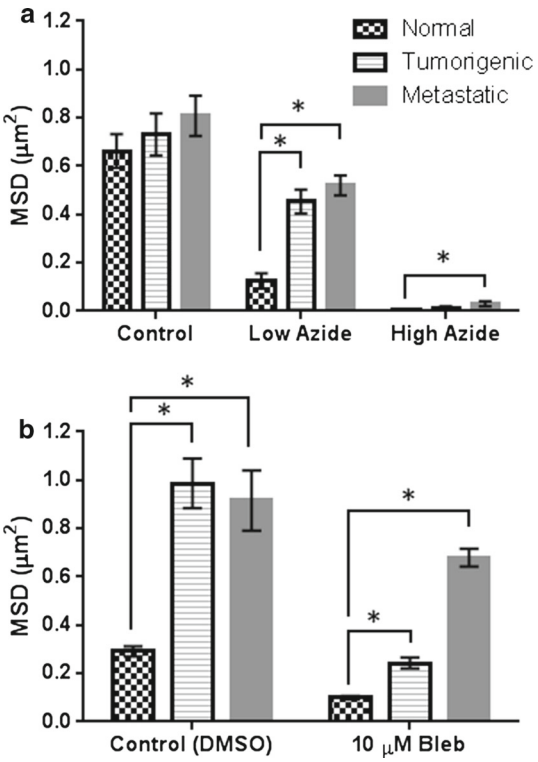

Fig. 5 Comparison of ensemble average peroxisome MSDs for $\tau = 90$ s in normal (*checkered*), tumorigenic (*striped*), and metastatic (*solid*) cells. **a** The three groups show MSDs in control cells, cells treated with low azide (2 mM sodium azide + 2 mM 2-deoxy-D-glucose), and cells treated with high azide (8 mM sodium azide + 50 mM 2-deoxy-D-glucose). **b** The two groups show the MSDs in control cells (with DMSO) and in cells treated with 10 μM (−)-blebbistatin. *Error bars* represent standard error of the mean (Eq. 6). The * represents a significant difference ($p < 0.005$)

3.4 The viscoelastic moduli of metastatic breast cells were lower than those in normal breast cells

To address the hypothesis that cancerous breast epithelial cells have lower viscoelastic moduli than their normal counterparts, peroxisome MSDs from normal and metastatic ATP-reduced cells were used to determine apparent moduli $|AM^*|$ and viscoelastic moduli $|G^*|$ from Eq. 2, the generalized Stokes–Einstein equation. Use of Eq. 2 requires that the MSDs of endogenous particles of ATP-reduced cells are dominated by thermally driven motion and that the cytoskeletal structure of the cells is not changed by the drug treatment. It has been suggested that convergence of the MSDs from drug-treated and untreated cells is evidence that drug treatment has not altered the cytoskeleton (Mizuno et al. 2007; Guo et al. 2014a). The MSDs of high-azide-treated and untreated cells did converge at small τ for the normal cells and the metastatic cells, but not for the tumorigenic cells (Fig. 3). In addition, the large reduction in ATP concentrations after high-azide treatment suggested that non-equilibrium peroxisome motions are largely suppressed in high azide. For these reasons, we have applied GSE analysis to the high-azide MSD data, obtaining the mechanical modulus G^* (Fig. 6d).

For the purpose of comparison, the MSDs in control, blebbistatin, and low-azide conditions were used to determine apparent moduli even though peroxisome motion in these conditions was still driven, to varying degrees, by ATP-powered processes. To avoid confusion with G^*, we use the symbol AM^*.

Table 1 p value results of the Mann–Whitney U test for differences between the MSD distributions of normal and tumorigenic cells, and of normal and metastatic cells, at $\tau = 90$ s

Treatment	Median MSD (μm^2) for $\tau = 90$ s			(1) p value for distributions	(2) p value for medians
	Normal	Tumorigenic	Metastatic		
Figure 5a					
Control	0.2730	0.3126		0.278	0.457
	0.2730		0.3257	0.483	0.273
Low Azide	0.0190	0.1626		**<0.005**	**<0.005**
	0.0190		0.1888	**<0.005**	**<0.005**
High Azide	0.0022	0.0025		0.480	0.420
	0.0022		0.0074	**<0.005**	**<0.005**
Figure 5b					
Control (DMSO)	0.1640	0.5061		**<0.005**	**<0.005**
	0.1640		0.3985	**<0.005**	**<0.005**
10 μM Bleb	0.0291	0.1236		**<0.005**	**<0.005**
	0.0291		0.2743	**<0.005**	**<0.005**

The last two columns in the table give (1) p values for comparing the distributions of MSDs for each pair of cell types, and (2) p values for comparing the median MSDs for each pair of cell types. Values in bold indicate a statistically significant difference ($p < 0.005$)

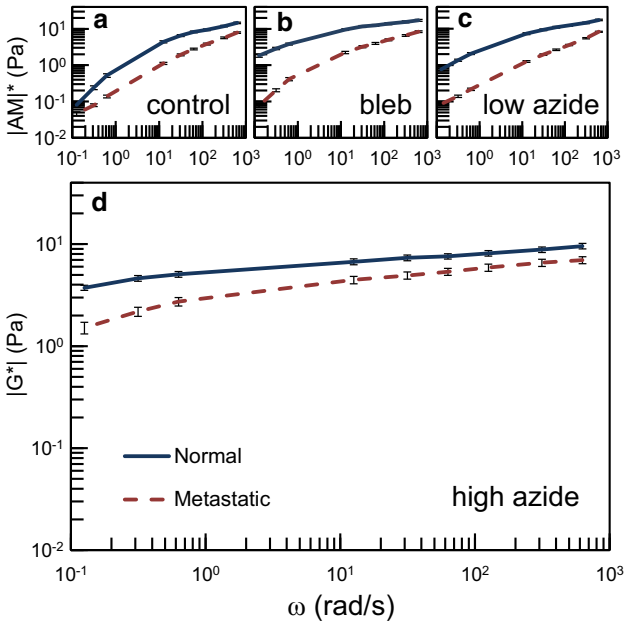

Fig. 6 Viscoelastic moduli ($|G^*|$) and apparent moduli ($|AM^*|$) of normal (*solid line*) and metastatic (*short dashed line*) breast cells determined from peroxisome MSDs. Cells were either **a** untreated, **b** treated with 10 μM (−)-blebbistatin for 15 min–1 h,) treated with low azide (2 mM sodium azide + 2 mM 2-deoxy-D-glucose) for 3–6 h, or **d** treated with high azide (8 mM sodium azide + 50 mM 2-deoxy-D-glucose) for 3–6 h. *Error bars* show standard error of the mean (Eq. 6)

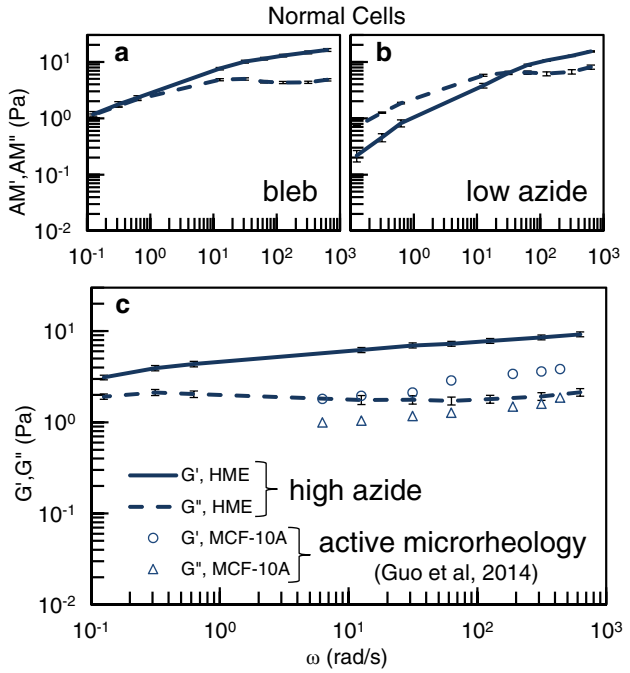

Fig. 7 Elastic (*solid line*) and viscous (*dashed line*) components of $|AM^*|$ and $|G^*|$ for normal breast cells treated with **a** 10 μM (−)-blebbistatin, **b** low azide, **c** high azide. The *circles* (◯) and *triangles* (△) are measurements of G' and G'' by active microrheology for beads in benign MCF-10A cells (Guo et al. 2014a). *Error bars* show the standard error of the mean

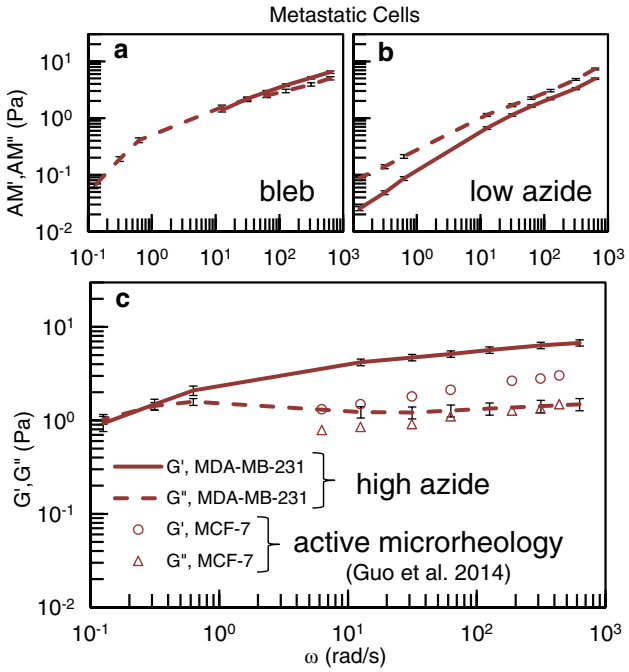

Fig. 8 Elastic (*solid line*) and viscous (*dashed line*) components of AM^* and G^* for metastatic breast cells treated with **a** 10 μM (−)-blebbistatin, **b** low azide, or **c** high azide. The *circles* (◯) and *triangles* (△) are measurements of G' and G'' by active microrheology of beads in malignant MCF-7 breast cells (Guo et al. 2014a). *Error bars* show the standard error of the mean

Figure 6 shows plots of $|G^*|$ and $|AM^*|$ for the normal and metastatic cell types and three treatments, as well as controls, for frequencies between 0.126 and 628 rad/s. The viscoelastic moduli increased from low shear frequencies to high shear frequencies in all cases. Treatment with azide or blebbistatin increased the apparent moduli by several orders of magnitude at low shear frequencies, flattening the curves. After treatment with high azide, curves for G^* were nearly flat. After partial inhibition of active processes (Fig. 6b, c), the apparent viscoelastic moduli of the metastatic cells were approximately an order of magnitude smaller than those of normal cells at low shear frequencies (e.g., $\omega = 0.126$ rad/s). The viscoelastic moduli of metastatic cells were approximately half those of normal cells at high shear frequencies (e.g., $\omega = 628.32$ rad/s). After treatment with high azide, the viscoelastic modulus of metastatic cells at $\omega = 0.126$ rad/s was half that of normal cells, and at $\omega = 628.32$ rad/s, still less than normal cells by more than the standard error. Thus, the intracellular viscoelastic moduli of metastatic cells were lower than normal cells, at all shear frequencies from 0.126 to 628 rad/s.

Figures 7 and 8 show the elastic and viscous moduli of AM^*, and G^* for normal and metastatic cells, respectively. In the presence of blebbistatin and low azide, AM' and AM'' showed strong dependence on ω for both cell types. For cells

treated with high azide, however, the curves for G' and G'' were flatter and the elastic modulus dominated over the viscous modulus at nearly all frequencies. The absolute values of G' and G'' were slightly lower for metastatic cells than for normal cells, confirming conclusions reached from the MSD curves.

As a test for the validity of our results, which required application of the GSE equation and ATP depletion, we added to Figs. 7 and 8 values of G' and G'' determined by active microrheology in two cell lines similar to our normal and metastatic cells (Guo et al. 2014a). These measurements do not use the GSE equation or drug treatment. We have converted Guo et al's values of the cytoplasmic spring constants K' and K'' to G' and G'' using the Stokes relation $K = 6\pi GR$, where R is the bead radius. The similarity of the values of G' and G'' obtained by active and passive microrheology supports the reliability of the mechanical properties we have measured.

4 Discussion

Peroxisome MSDs in untreated cells determined here are comparable to MSDs in previous studies of similar cell types (Table 2). The effects of a variety of drug treatments on MSDs of particles in the interior of breast cells have also been studied previously (Goldstein et al. 2013). The purpose of that study was to understand mechanisms of particle transport; viscoelastic moduli were not reported.

A recent study by Guo et al. (2014a) uses active microrheology to determine the mechanical properties of several cell lines. Laser tweezers are used to oscillate microinjected 500 nm beads in the cytoplasm. The responses of the beads allow the calculation of G' and G'' without invoking the GSE equation. The values of G' and G'' obtained for MCF-10A (benign) and MCF-7 (malignant) breast cells are shown in Figs. 7 and 8. The log–log slopes of G' for our normal and metastatic cells, 0.10 and 0.12, are similar to those in the MCF-10A and MCF-7 cells, 0.19 and 0.20. Noting that the cell lines are not identical, the agreement between G' and G'' measurements acquired by passive microrheology in ATP-depleted cells and active microrheology in untreated cells supports the validity of our use of passive microrheology and the GSE equation if ATP depletion is carefully executed.

While our MSDs are comparable to MSDs previously determined by particle-tracking experiments in breast cells, our values of G are several orders of magnitude smaller than measurements by AFM indentation (500–2000 Pa) even on the same cell types (Li et al. 2009; Lee et al. 2012; Network TPS-OC 2013; Guo et al. 2014b). The discrepancy probably arises because these techniques probe distinct structures within the cell. The poroelastic model of cell mechanics provides one way to bring the two results together into a

Table 2 Comparison of MSDs of particles in untreated breast Cells

Breast cell type	Author	Probe size	Probe introduction method	Tau range (s)	MSD range (μm^2)
HMEC (benign, not immortalized)	This work	~ 400 nm	Endogenous[a]	0.01–90	0.0008–0.7
MCF-10A (benign)	Guo et al. (2014b)	500 nm	Microinjection	0.01–20	0.002–0.02
	Network TPS-OC (2013)	100 nm	Ballistic Injection	0.03–10	0.0004–0.05
	Gal and Weihs (2012)	200 nm	Endocytosis	0.02–60	0.00002–0.1
	Li et al. (2009)	≈ 500 nm	Endogenous[b]	0.04–9	0.001–0.009
		200 nm	Ballistic injection	0.04–20	0.0007–0.03
HMLER (tumorigenic)	This work	~ 400 nm	Endogenous[a]	0.01–90	0.001–0.7
MCF-7 (tumorigenic)	Guo et al. (2014a)	500 nm	Microinjection	0.01–20	0.002–0.07
	Li et al. (2009)	≈ 500 nm	Endogenous[b]	0.04–7	0.002–0.2
		200 nm	Ballistic injection	0.04–20	0.002–0.6
MDA-MB-468 (low metastatic)	Goldstein et al. 2013	200 nm	Endocytosis	0.02–60	0.00003–0.2
	Gal and Weihs (2012)	200 nm	Endocytosis	0.02–60	0.00003–0.2
MDA-MB-231 (high metastatic)	Network TPS-OC (2013)	100 nm	Ballistic Injection	0.03–10	0.0004–0.2
	Goldstein et al. (2013)	200 nm	Endocytosis	0.02–60	0.0001–0.7
	Gal and Weihs (2012)	200 nm	Endocytosis	0.01–60	0.0001–1
	This work	~ 400 nm	Endogenous[a]	0.01–90	0.001–0.8

[a] Peroxisomes, [b] Lipid granules

single "two-phase" model. In this model, particle-tracking microrheology measures the properties of the viscoelastic fluid phase which can flow between interconnected pores within the elastic cytoskeletal mesh phase. AFM and magnetic twisting cytometry, which indent or displace the cell membrane from outside the cell, measure the modulus of the mesh phase. Confocal and electron microscopy images of cells show a mesh of closely spaced actin fibers close to the cell membrane (Heuser and Kirschner 1980; Burnette et al. 2014). Projection confocal images of our MDA-MB-231 cells showed an average spacing of approximately 0.9 μm between fluorescently labeled actin stress fibers (L. McDonald and G. Holzwarth, unpublished), whereas the diameter of peroxisomes in these cells was ∼ 0.4 μm. This suggests that peroxisomes are small enough to move through the pores between the stiff actin fibers, which behave like an elastic solid.

The slopes of our log MSD versus log τ curves (Figs. 3 and 4) were close to 0 for small values of τ but increased to 1 for large values of τ. Such behavior is common in concentrated solutions of high MW polymers and is explained by constraint release (Doi and Edwards 1988), that is, at short times, polymer chains are entangled with one another, so they behave like a cross-linked elastic solid. However, over long times, the chains can reptate around one another, releasing the entanglement restraints and thus allowing an increase in diffusion for a suspended probe particle. The mesh of stiff cytoskeletal fibers may behave similarly, trapping the peroxisome on a short time scale, but releasing the peroxisome from its trap of cytoskeletal fibers over longer times. The data for normal cells (Fig. 7) suggest that the constraint release time is roughly 0.1 s.

The ATP- and myosin II-dependent random motion of particles within cells is usually explained as an indirect result of ATP- and myosin II-dependent cytoskeletal motions (Bursac et al. 2005; Hoffman et al. 2006; Van Citters et al. 2006; Bursac et al. 2007; Brangwynne et al. 2008; Gallet et al. 2009; Brangwynne et al. 2009). An alternative hypothesis is that such motion, especially for endogenous particles such as peroxisomes, is the direct result of multiple competing myosins attaching each peroxisome to multiple actin filaments with different orientations, with the result that the peroxisome is pulled in different directions at different times (D. Lyles, personal communication, 2014). Whichever explanation is true, if active intracellular processes contribute to probe MSDs, a central assumption of GSE analysis is violated.

In control, low azide, or blebbistatin conditions, the average peroxisome MSD of tumorigenic cells at the longest value of τ (90 s) was higher than that of normal cells. This suggests that one or more of the three genes *hTERT*, oncogenic H-*ras*V12, and the SV40 large-T oncogene transfected into HME cells to transform them into HMLERs led to increased peroxisome motion. Because the peroxisome MSDs for untreated and treated tumorigenic cells did not converge, this increased motion could be explained at least partly by increased motor activity, as compared to normal cells. This conclusion is supported by Fig. 5a, which shows that the average peroxisome MSD in tumorigenic cells was not significantly higher than that of normal cells when both were treated with high azide. Of the three genes transfected into the HMLERs, H-RasV12 would be the most likely candidate responsible for increased motor activity because it is upstream of MLCK, which activates myosin binding to actin. Experiments comparing peroxisome motion in breast cells differing only in Ras activity would need to be performed to confirm this hypothesis.

One difficulty in attempting to reduce the effect of active intracellular processes on peroxisome MSD measurements is the fact that depleting cells of ATP using sodium azide and 2-deoxy-D-glucose could lead to rearrangements of the actin (Atkinson et al. 2004; Van Citters et al. 2006; Mizuno et al. 2007; Guo et al. 2014a). Because perfect inhibition of active processes and preservation of the cytoskeleton are difficult to simultaneously achieve in cells, the optimal balance may be to titrate active process inhibitors until changes in mechanics become just detectable. Toward this end, we have explored two levels of ATP inhibition (low and high azide) as well as multiple levels of the motor-specific inhibitor, blebbistatin. Blebbistatin only partially reduced ATP-driven motion in our cells. Treatment with low azide, while sufficient to reduce ATP levels to 2–7 % of controls in HASM cells (Bursac et al. 2005), did not reduce ATP levels in the breast epithelial cells studied here nearly as much (81–130 % of controls). Treatment with high azide, on the other hand, reduced ATP levels to 1–8 % in our cells. While cells undergoing this treatment did round up, average peroxisome MSDs converged to those of untreated cells at short values of τ, suggesting that any cytoskeletal changes that may have occurred did not affect peroxisome motion.

5 Conclusions

The elastic and viscous shear moduli (G', G'') of interior regions of live normal and metastatic breast cells were determined by passive microrheology for shear rates between 0.126 and 628 rad/s. The moduli were computed from MSDs of peroxisomes in the cells, following careful reduction in non-thermal, ATP- or myosin-dependent motions by treatment of the cells with sodium azide and deoxyglucose or blebbistatin. The shear moduli measured in this way were significantly reduced for metastatic cells as compared to normal cells, especially at low shear rates. The elastic modulus was almost always significantly larger than the loss modulus. Both the shear modulus for the cell interior, as reported here, and the elastic modulus of the actin cortex, which is

commonly measured by AFM, determine the rate of stress relaxation following indentation of cells (Moeendarbary et al. 2013). For this reason, the measured values reported here for the interior viscoelastic regions of normal and metastatic breast cells define key parameters for the development of quantitative mechanical models of cell deformation during metastasis.

Acknowledgments The authors thank K. Scarpinato and J. Jarzen for providing HMLER cells and insights on their culture, S. Fahrbach for the use of her luminometer for ATP assays, and L. McDonald and G. Marrs for high-resolution confocal fluorescence microscopy images of actin stress fibers in breast epithelial cells. The authors thank D. Lyles for comments on this manuscript. This material is based upon work supported by the National Science Foundation under Grant Number 1106105 (JM, KB, and GH). AMS was supported by National Institutes of Health (T32GM095440) and National Science Foundation (0907738) Grants.

References

Allingham JS, Smith R, Rayment I (2005) The structural basis of blebbistatin inhibition and specificity for myosin II. Nat Struct Mol Biol 12:378–379. doi:10.1038/nsmb908

Atkinson SJ, Hosford MA, Molitoris BA (2004) Mechanism of actin polymerization in cellular ATP depletion. J Biol Chem 279:5194–5199. doi:10.1074/jbc.M306973200

Bertseva E, Grebenkov D, Schmidhauser P et al (2012) Optical trapping microrheology in cultured human cells. Eur Phys J E 35:63. doi:10.1140/epje/i2012-12063-4

Brangwynne CP, Koenderink GH, MacKintosh FC, Weitz DA (2008) Cytoplasmic diffusion: molecular motors mix it up. J Cell Biol 183:583–587. doi:10.1083/jcb.200806149

Brangwynne CP, Koenderink GH, MacKintosh FC, Weitz DA (2009) Intracellular transport by active diffusion. Trends Cell Biol 19:423–427. doi:10.1016/j.tcb.2009.04.004

Burnette DT, Shao L, Ott C et al (2014) A contractile and counterbalancing adhesion system controls the 3D shape of crawling cells. J Cell Biol 205:83–96. doi:10.1083/jcb.201311104

Bursac P, Fabry B, Trepat X et al (2007) Cytoskeleton dynamics: fluctuations within the network. Biochem Biophys Res Commun 355:324–330. doi:10.1016/j.bbrc.2007.01.191

Bursac P, Lenormand G, Fabry B et al (2005) Cytoskeletal remodelling and slow dynamics in the living cell. Nat Mater 4:557–561. doi:10.1038/nmat1404

Butcher DT, Alliston T, Weaver VM (2009) A tense situation: forcing tumour progression. Nat Rev Cancer 9:108–122. doi:10.1038/nrc2544

Choi C, Helfman DM (2013) The Ras-ERK pathway modulates cytoskeleton organization, cell motility and lung metastasis signature genes in MDA-MB-231 LM2. Oncogene. doi:10.1038/onc.2013.341

Doi M, Edwards SF (1988) The theory of polymer dynamics. Oxford University Press, Oxford

Elenbaas B, Spirio L, Koerner F et al (2001) Human breast cancer cells generated by oncogenic transformation of primary mammary epithelial cells. Genes Dev 15:50–65. doi:10.1101/gad.828901

Gallet F, Arcizet D, Bohec P, Richert A (2009) Power spectrum of out-of-equilibrium forces in living cells?: amplitude and Frequency Dependence. Soft Matter 5:2947–2953. doi:10.1039/b901311c

Gal N, Weihs D (2012) Intracellular mechanics and activity of breast cancer cells correlate with metastatic potential. Cell Biochem Biophys 63:199–209. doi:10.1007/s12013-012-9356-z

Gal N, Lechtman-Goldstein D, Weihs D (2013) Particle tracking in living cells: a review of the mean square displacement method and beyond. Rheol Acta 52:425–443. doi:10.1007/s00397-013-0694-6

Goldstein D, Elhanan T, Aronovitch M, Weihs D (2013) Origin of active transport in breast-cancer cells. Soft Matter 9:7167–7173. doi:10.1039/C3SM50172H

Grebenkov DS (2011) Probability distribution of the time-averaged mean-square displacement of a Gaussian process. Phys Rev E 84:031124. doi:10.1103/PhysRevE.84.031124

Guo M, Ehrlicher AJ, Jensen MH et al (2014a) Probing the stochastic, motor-driven properties of the cytoplasm using force spectrum microscopy. Cell 158:822–832. doi:10.1016/j.cell.2014.06.051

Guo X, Bonin K, Scarpinato K, Guthold M (2014b) The effect of neighboring cells on the stiffness of cancerous and non-cancerous human mammary epithelial cells. New J Phys 16:105002. doi:10.1088/1367-2630/16/10/105002

Guo M, Ehrlicher AJ, Mahammad S et al (2013) The role of vimentin intermediate filaments in cortical and cytoplasmic mechanics. Biophys J 105:1562–1568. doi:10.1016/j.bpj.2013.08.037

Heuser JE, Kirschner MW (1980) Filament organization revealed in platinum replicas of freeze-dried cytoskeletons. J Cell Biol 86:212–234

Hoffman BD, Massiera G, Van Citters KM, Crocker JC (2006) The consensus mechanics of cultured mammalian cells. Proc Natl Acad Sci USA 103:10259–10264. doi:10.1073/pnas.0510348103

Ishikawa T, Zhu B-L, Maeda H (2006) Effect of sodium azide on the metabolic activity of cultured fetal cells. Toxicol Ind Health 22:337–341. doi:10.1177/0748233706071737

Kovacs M, Toth J, Hetenyi C et al (2004) Mechanism of blebbistatin inhibition of myosin II. J Biol Chem 279:35557–35563. doi:10.1074/jbc.M405319200

Kural C, Kim H, Syed S et al (2005) Kinesin and dynein move a peroxisome in vivo: a tug-of-war or coordinated movement? Science 308:1469–1472. doi:10.1126/science.1108408

Lee M-H, Wu P-H, Staunton JR et al (2012) Mismatch in mechanical and adhesive properties induces pulsating cancer cell migration in epithelial monolayer. Biophys J 102:2731–2741. doi:10.1016/j.bpj.2012.05.005

Lemmon EW (2014) Thermophysical Properties of Water and Steam. In: Haynes WM (ed) Handb. Chem. Phys. Online, 94th edn. Taylor and Francis, London, pp 6–1. http://www.hbcpnetbase.com. Accessed 29 April 2014

Limouze J, Straight AF, Mitchison T, Sellers JE (2004) Specificity of blebbistatin, an inhibitor of myosin II. J Muscle Res Cell Motil 25:337–341. doi:10.1007/s10974-004-6060-7

Li Y, Schnekenburger J, Duits MHG (2009) Intracellular particle tracking as a tool for tumor cell characterization. J Biomed Opt 14:064005. doi:10.1117/1.3257253

Mason TG (2000) Estimating the viscoelastic moduli of complex fluids using the generalized Stokes–Einstein equation. Rheol Acta 39:371–378. doi:10.1007/s003970000094

Mizuno D, Tardin C, Schmidt CF, MacKintosh FC (2007) Nonequilibrium mechanics of active cytoskeletal networks. Science 315:370–373. doi:10.1126/science.1134404

Moeendarbary E, Valon L, Fritzsche M et al (2013) The cytoplasm of living cells behaves as a poroelastic material. Nat Mater 12:253–261. doi:10.1038/NMAT3517

Nagaraja GM, Othman M, Fox BP et al (2006) Gene expression signatures and biomarkers of noninvasive and invasive breast cancer cells: comprehensive profiles by representational difference analysis, microarrays and proteomics. Oncogene 25:2328–2338. doi:10.1038/sj.onc.1209265

Network TPS-OC (2013) A physical sciences network characterization of non-tumorigenic and metastatic cells. Sci Rep. doi:10.1038/srep01449

Paszek MJ, Zahir N, Johnson KR et al (2005) Tensional homeostasis and the malignant phenotype. Cancer Cell 8:241–254. doi:10.1016/j.ccr.2005.08.010

Pratt JW, Gibbons JD (1981) Concepts of nonparametric theory. Springer, New York

Rapp S, Saffrich R, Jakle U et al (1996) Microtubule-mediated peroxisomal saltations. Ann NY Acad Sci 804:666–668

Saxton MJ (1997) Single-particle tracking: the distribution of diffusion coefficients. Biophys J 72:1744–1753

Schedin P, Keely PJ (2011) Mammary gland ECM remodeling, stiffness, and mechanosignaling in normal development and tumor progression. Cold Spring Harb Perspect Biol 3:a003228. doi:10.1101/cshperspect.a003228

Schrader M, King SJ, Stroh TA, Schroer TA (2000) Real time imaging reveals a peroxisomal reticulum in living cells. J Cell Sci 113:3663–3671

Schrader M, Thiemann M, Fahimi HD (2003) Peroxisomal motility and interaction with microtubules. Microsc Res Tech 61:171–178. doi:10.1002/jemt.10326

Squires TM, Mason TG (2010) Fluid mechanics of microrheology. Annu. Rev. Fluid Mech. Annual Reviews, Palo Alto, pp 413–438

Suresh S (2007) Biomechanics and biophysics of cancer cells. Acta Biomater 3:413–438. doi:10.1016/j.actbio.2007.04.002

Van Citters KM, Hoffman BD, Massiera G, Crocker JC (2006) The role of F-actin and myosin in epithelial cell rheology. Biophys J 91:3946–3956. doi:10.1529/biophysj.106.091264

Wick AN, Drury DR, Nakada HI, Wolfe JB (1957) Localization of the primary metabolic block produced by 2-deoxyglucose. J Biol Chem 224:963–969

Wiemer E a C, Wenzel T, Deerinck TJ et al (1997) Visualization of the peroxisomal compartment in living mammalian cells: dynamic behavior and association with microtubules. J Cell Biol 136:71–80. doi:10.1083/jcb.136.1.71

Wirtz D (2009) Particle-tracking microrheology of living cells: principles and applications. Annu Rev Biophys 38:301–326. doi:10.1146/annurev.biophys.050708.133724

Zhang B, Zerubia J, Olivo-Marin J-C (2007) Gaussian approximations of fluorescence microscope point-spread function models. Appl Opt 46:1819–1829